ANALYSIS OF MELT POOL DURING THE LASER POWDER BED FUSION OF TUNGSTEN

A.T. Sidambe[1*] & P. Fox[2]

[1]Department of Mechanical, Materials & Aerospace Engineering, University of Liverpool, United Kingdom
a.sidambe@liverpool.ac.uk

[2]Department of Mechanical, Materials & Aerospace Engineering, University of Liverpool, United Kingdom
foxp@liverpool.ac.uk

ABSTRACT

Laser powder bed fusion is a leading additive manufacturing technology which has been used in this study to melt pure tungsten powder onto a titanium substrate. A strategy for the powder bed fusion was carried out by creating a process map in which the effect of laser energy density on the melt pool was studied. Our approach was to consider the laser focus offset as a control parameter in the experimental work, with melting carried out before and after the Gaussian laser beam profile was optimised. The optimal focus offset was achieved at 1 mm, yielding a laser beam diameter (the effective gaussian laser beam radius at which the maximum irradiance is decayed to $1/e^2$ or 13.5% of the peak value) of 43 µm at the target surface. Before laser beam focusing, the beam diameter was 50 µm. The selective laser melting of the tungsten powder on the titanium substrate was carried out by melting single layer melt tracks using laser power ranges of 100, 150 and 200W and laser speeds ranging from 50 to 400 mm/s before and after the Gaussian laser beam profile was optimised. The results showed that optimised parameters were able to melt the W and create a strong bond on a CPTi substrate. Keyhole mode and conduction mode were observed under different linear energy densities.

[1] Department of Mechanical, Materials & Aerospace Engineering, University of Liverpool, United Kingdom
[2] Department of Mechanical, Materials & Aerospace Engineering, University of Liverpool, United Kingdom
*Corresponding author

ISBN 978-0-6398390-0-4

1. INTRODUCTION

Laser powder bed fusion (LPBF) is an additive manufacturing (AM) process used by various industry sectors to lower the cost of production for high value low volume manufacturing and for complex shapes. LPBF is emerging as an alternative to conventional methods such as machining and casting (Sidambe et al. [1]). In LPBF, a high-powered laser is used to fuse metal powder into a solid component using data from a sliced 3D CAD file, one layer at a time. The layer thickness is typically in the range of 30 µm to 50 µm. More details of LPBF have been published by Sidambe [2].

Tungsten (W) is a metal which is ideally used in ultra-high temperature and shielding applications within many technology fields such as military, electro vacuum, crucible, heating elements and pinhole collimators (Deprez et al. [3], Sidambe et al. [4]). The processing of pure tungsten using LPBF is difficult because tungsten has a high thermal conductivity, high melting temperature and a ductile-to-brittle transition temperature which renders tungsten susceptible to cracking (Braun et al. [5],Wang et al. [6], Li et al. [7]).

Table 1 shows the physical properties of tungsten, and of particular interest are the comparatively high viscosity, high density, high melting point and the high thermal conductivity which are expected to contribute to the difficulties of processing tungsten via LPBF. In comparison, the thermal conductivity of titanium is 16.4 $W.m^{-1}.K^{-1}$ and that of stainless steel is 15 $W.m^{-1}.K^{-1}$. The high melting point of tungsten has been reported to contribute to a high cohesive energy and high surface tension, which in turn leads to high melt viscosity in LPBF (Zhou et al. [8]), whereas the ductile-to-brittle transition temperature (DBTT) renders tungsten susceptible to cracking from the build-up of residual stresses (Zhou et al. [8], Wang et al. [9]).In addition to the above mentioned properties, the processing of tungsten using LPBF is also made difficult by the complexity of the LPBF process and its non-equilibrium nature which requires an in-depth understanding of the process (Rombouts et al. [10]).

Table 1: Physical properties of tungsten.

Physical Properties	Tungsten
Density at 25 °C (g/cm^3)	19.2
Liquid Density (g/cm^3)	17.6
Melting Point (°C)	3422
Thermal Conductivity ($W.m^{-1}.K^{-1}$)	174
Surface tension Force (N/m)	2.361
Melt viscosity (mPa.s)	8
Ductile-to-brittle transition temperature (°C)	250-400
Surface tension force (N/m)	2.361

However, although technically challenging, processing of tungsten via LPBF is expected to lead to an advantage in the high value manufacturing sectors such as medical implants, rocket nozzles and support hardware because LPBF has the ability to manufacture complicated shaped tungsten parts with small dimensions, something which cannot be achieved using traditional metal working techniques such as milling, casting or pressing because of the hardness and strength of tungsten (Deprez et al. [3], Zhou et al. [8], Wauthle et al. [11], Müller et al. [12]).

In order to overcome the challenges of manufacturing tungsten components using conventional methods, there have been a number of studies carried out to investigate the use of additive manufacturing. In an early investigation, Ebert et al. [13] used pulsed-laser micro sintering and demonstrated that the final density of tungsten parts increased with the applied laser energy. A year later, Deprez et al. [3] successfully fabricated a more complex MR-compatible collimator with a large number of oblique pinholes from pure tungsten powder using LPBF. More recently (Zhou et al. [8], Nie et al. [13], Bai et al. [14], Ivekovic et al. [15], Tan et al. [16], Yang et al. [17], Guo et

al. [18]), the intrinsic physical properties of tungsten properties and the laser processing parameters have been established as being important in determining the properties of parts produced by the LPBF process. These studies also identified oxidation as a phenomenon that can hinder successful tungsten LPBF processing, which must be avoided. Gear et al. [19],[20] showed that the LPBF processing parameters such as the scanning strategy can have an influence on the radiation attenuation properties of pure tungsten used in pinhole collimators.

In this study, we expand on the results from our developmental work (Sidambe et al. [1],[4],[21],[22]) to carry out an analysis of the melt spreading and solidification of tungsten in relation to LPBF parameters and explain the mechanisms in terms of the tungsten melt pool and the titanium substrate properties. By discussing the mechanism of the formation of the melt pool during the LPBF of tungsten, we elaborate on the effect of the tungsten properties. According to studies that have been published on the formation of the melt pool and the relationship with mechanisms such as surface tension (Karapatis [23], Niu et al. [24], Kruth et al. [25], Guo et al. [26]), the selection of the laser parameters should be such that the length to diameter ratio of the molten pool is as small as possible. Our study considered the use of low and high scan speeds in combination with a range of laser powers, and we report on the effect of these combinations on the formation of the tungsten melt pool on a titanium base plate.

2. METHODOLOGY

A Renishaw AM125 laser powder bed fusion machine was used in this study. Due to the challenges in melting tungsten it is essential to achieve the maximum irradiance of the laser during processing. Our approach was therefore also to consider the laser focus offset as a control parameter, with melting carried out before and after the Gaussian laser beam profile was optimised. The optimisation of the Gaussian laser beam (or laser spot) profile was carried out using an Ophir Photonics Spiricon SP620 beam profiler. Figure 1 shows the irradiance and laser beam diameter distribution during the laser beam profiling. The optimal focus offset was achieved at 1 mm, yielding a laser beam diameter (the effective laser beam radius at which the maximum irradiance is decayed to $1/e^2$ or 13.5% of the peak value (Alda [27])) of 43 µm. At the laser focus offset of 0 mm, laser beam diameter was 50 µm. The Gaussian power density distribution of the laser beam irradiance and the beam diameter at 200W during the beam profiling is illustrated in Figure 2. The calculations showed that there was an increase of 25% in the peak intensity due to the smaller laser beam diameter of 45 µm.

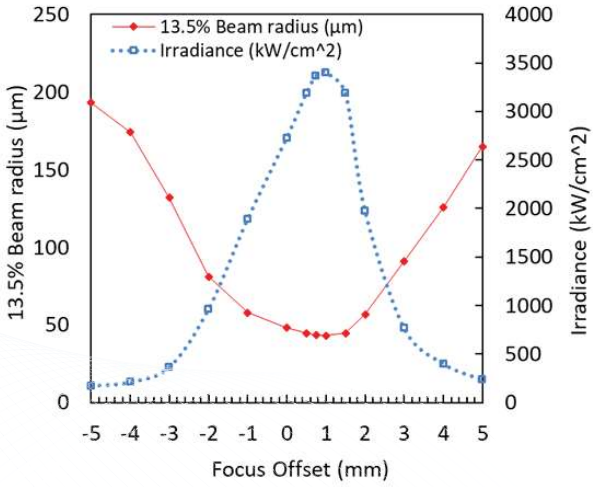

Figure 1: Irradiance and laser beam diameter distribution during the laser beam profiling (Sidambe et al. [22]).

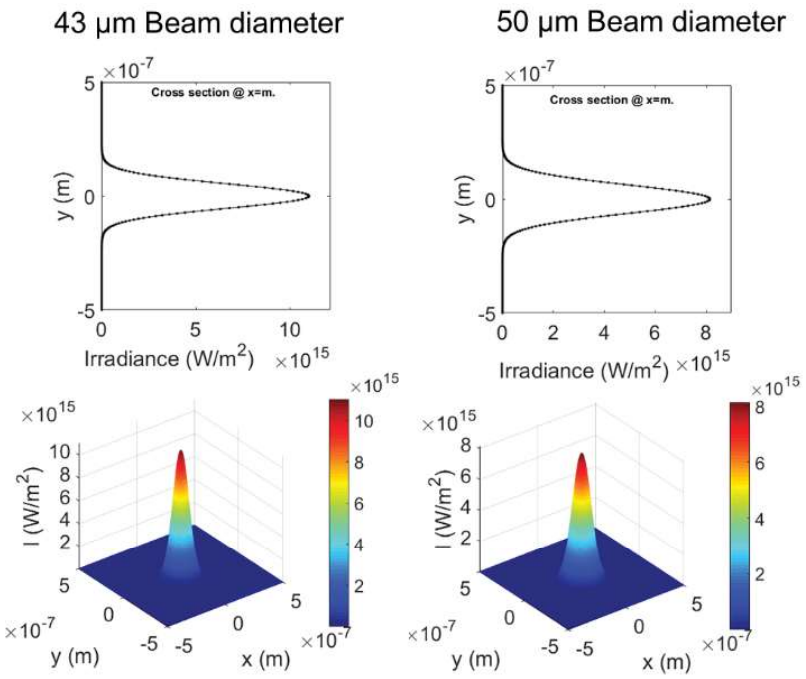

Figure 2: Gaussian power density distribution showing the laser beam diameter of 43 µm at 1mm offset, and 50 µm at 0 mm offset.

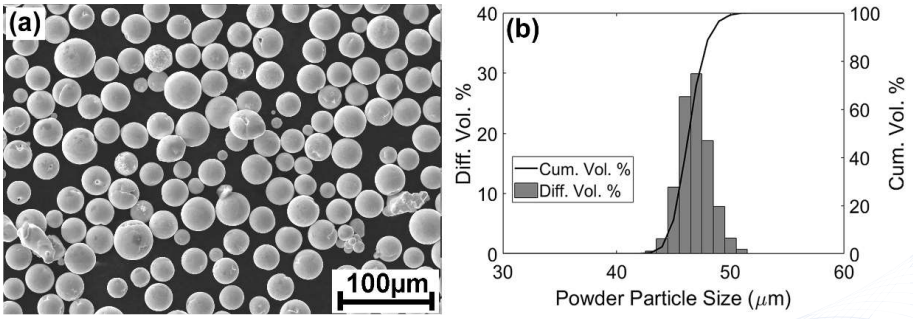

Figure 3: (a) Scanning electron micrograph showing the highly spherical morphology of the tungsten powder, (b) powder particle distribution for tungsten.

The tungsten power used in the study was Plasma-spheroidised, hence it was highly pure and highly spherical. Figure 3 (a) shows the highly spherical morphology of the tungsten powder and also shown in Figure 3 (b) is the powder particle size distribution. The tungsten powder melting was carried out under an argon atmosphere with an initial residual oxygen content of less than 800 ppm (0.08%) on the Renishaw AM125 system. A commercially pure titanium (CPTi) Grade 4 substrate was used for

the LPBF experiments. Careful considerations were given in selecting titanium because the substrate and its thermal properties have been reported to have a significant effect on the LPBF process, particularly by influencing the nucleation of the melt pool and the solidification rate in initial layer (Müller et al. [12], Guo et al. [26]). The melting of the first layer of metallic powder in LPBF requires the melting of the substrate, leading to the mixing of the alloys within the melt pool. The usual practice is to use the same material for the substrate as the powder. However, it is considered to be commercially not viable to use a tungsten substrate in LPBF. Furthermore, because of the high melting point of tungsten makes it difficult to create a strong bonding on such a substrate.

Single layer melt tracks were melted using laser power range of 100, 150 and 200 W and laser scan speeds ranging from 50 mm/s to 400 mm/s (at increments of approximately 5 mm/s) before and after the laser beam profile was optimised. The two dimensional (2D) linear input laser energy (defined as the laser power per laser scan speed per line area) was calculated by combining laser power, laser scan speed and laser beam diameter (Brown [28]).

$$\mathcal{E}_{2D} = \boldsymbol{P_{Laser}}/\left(\boldsymbol{v_{scan}} \cdot \boldsymbol{\phi_{Spot}}\right) \qquad \textbf{Equation 1}$$

$\mathcal{E}_{2D}$ = 2D linear input laser energy density, P_{laser} = laser power, v_{scan} = the laser scan speed and ϕ_{Spot} = laser beam diameter. The resultant 2D linear laser energy density ranged from 5 J/mm^2 to 93 J/mm^2. The melt track and melt pool width, depth and overlap were analysed and quantified using the light optical microscopy (LOM) and ImageJ image processing software.

3. RESULTS

3.1 Melt Width

Figure 4, Figure 5 and Figure 6 show the results of the laser melting of single track, single layer tungsten powder on the titanium substrate. Figure 4 shows the quantification of the melted track width for the tungsten/CPTi as a function of the 2D linear laser energy density and shows the range of the line width (100 µm to 470 µm). It was confirmed that the geometrical dimensions of the melt tracks were dependent on the linear energy density as shown in Figure 4. The optimised laser beam had the effect of increasing the achievable maximum laser energy density as expected. At the lower energy densities, the melt track width was less varied when the laser beam diameter of 43 µm was used than when the laser beam diameter of 50 µm was used to melt the tungsten powder on titanium. Conversely as the laser energy density increased, the melt tracks were wider at the focus offset of 1 mm than at 0 mm. This was attributable to the melt viscosity which is thought to have been within the range that prompts sufficient melt spreading via a mode of heat transfer. The results indicate the presence of the well-known phenomenon where the surface tension coefficient as well as the melt viscosity decrease with increasing temperature induced by an increasing laser energy density (Yadroitsev et al. [29]). This useful information can be used to define the threshold for the energy density and study the effects on surface tension during the LPBF process.

Figure 5 is a plot of the laser power as a function of the laser speed for the optimised laser beam, (i.e. laser beam diameter = 43 µm and focus offset = 1 mm). Figure 5 shows that the geometrical dimensions of the melt tracks were dependent on scan speed and laser power. The optical micrographs in Figure 6 show an example of melt pool breakup with balling (left) and radially flattened (right) and broad tungsten and titanium (W+Ti) pool, (i.e. laser beam diameter = 43 µm and focus offset = 1 mm). When the 2D linear energy density was insufficient, i.e. when the laser power was lowered and the laser speed increased; this resulted in poor spreading of the melt tracks accompanied by melt break up which led to discontinuous melt tracks. With the increase of energy input which was achieved by increasing the laser power, lowering the laser scanning speed and decreasing the spot size, continuous melt tracks of increased width were formed. When the linear energy density was increased, the heat affected zone was increased, thereby eliminating the breakup of the melt leading to an increase in melt track width.

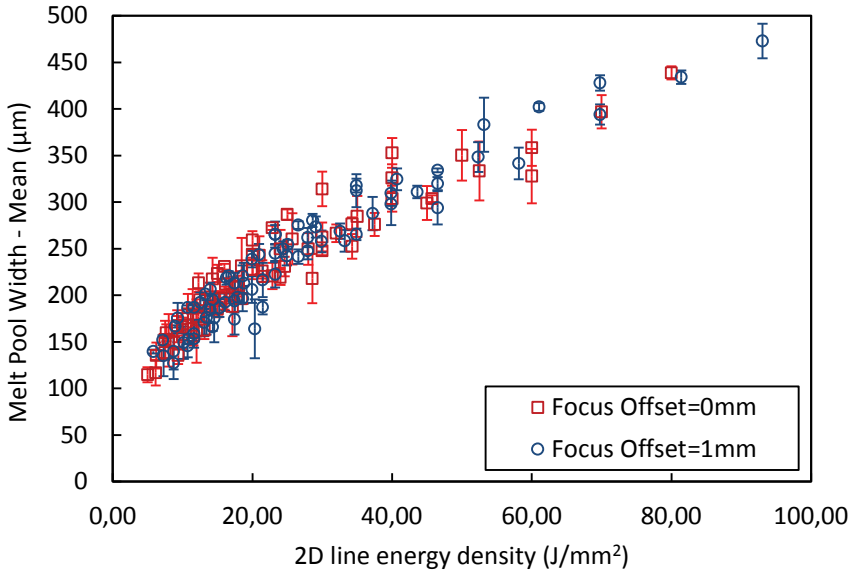

Figure 4: Melt pool width vs 2D linear laser energy density for tungsten powder on Ti before and after laser beam profile optimization.

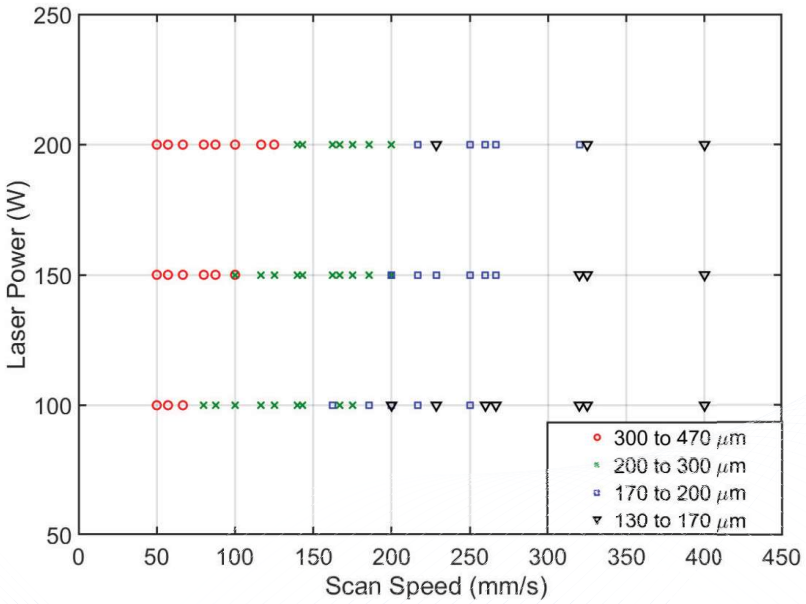

Figure 5: Range of melt track widths for tungsten on Ti achieved for the laser beam diameter of 43 µm.

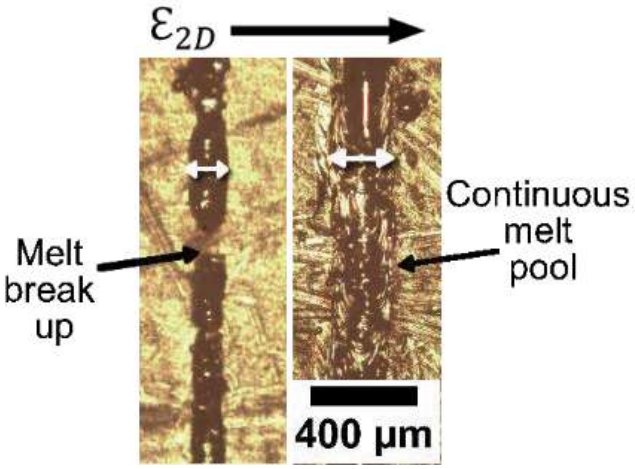

Figure 6: Optical micrographs showing an example of melt pool break up with balling (left) and radially flattened and broad tungsten pool (right) on a titanium substrate.

3.2 Melt Pool Height

Figure 7, Figure 8 and Figure 9 show the results of the penetration depth and melt pool height (heat affected zone - HAZ) for the tungsten power melted onto the titanium substrate. Figure 7 shows the quantification of the melt pool height for the tungsten/CPTi as a function of the 2D linear laser energy density and shows the range of the melt pool height (60 µm to 740 µm) for the laser beam diameter = 43 µm and focus offset = 1 mm.

The geometrical dimensions of the melt pool were also dependent on the linear energy density, but to a lesser extent compared to the dependence of the melt track width (Section 3.1). In this case, high levels of penetration depth and melt pool height were also achieved at lower energies of 40 J/mm^2. This can be explained by higher penetration depths and melt pool heights being also obtained where the scanning speed was high. The penetration depths and melt pool height measurements and results were recorded after the optimization of the laser beam. However, it is expected that the focus offset optimization should have the effect of increasing the penetration depth and melt pool height because the achievable maximum laser energy density was increased, as mentioned earlier. In the results, keyhole melt pool morphology mode and conduction mode were observed under different linear energy densities.

Figure 8 shows the range of melt pool height achieved for the laser beam diameter of 43 µm at laser powers of 100W, 150W and 200W as a function of the scanning speed. The conduction mode melt pool formation was mainly observed for the heights of 218 µm to 343 µm and the keyhole mode was observed where the melt pool penetration depths and height ranged from 347 µm to 740 µm.

Figure 9 shows the melt pool cross-sections after melting a layer of tungsten powder on a titanium substrate (laser beam diameter = 43 µm and focus offset = 1 mm). Increasing the laser energy density increased the melt pool total height and penetration depth, with the occurrence of some porosity in the keyhole mode. The effect of melting in titanium was that the tungsten is not completely melted initially but the titanium acts as a catalyst for initiating the melting of tungsten for the subsequent layers.

ISBN 978-0-6398390-0-4

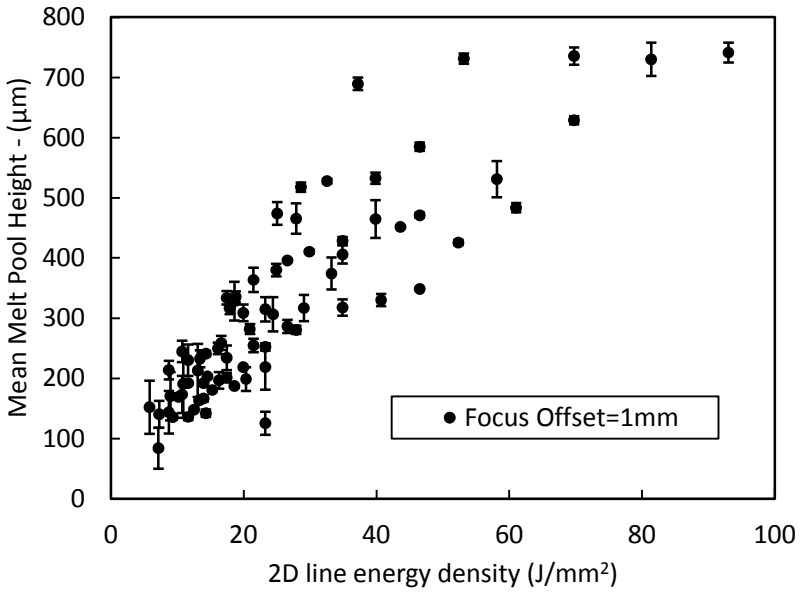

Figure 7: Plot of the melt pool height vs 2D linear laser energy density for tungsten powder after laser beam profile optimization (focus offset=1).

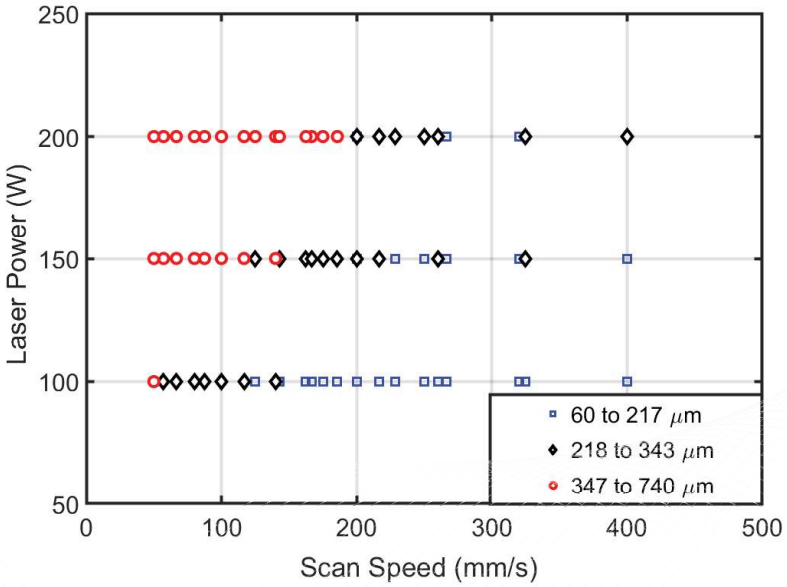

Figure 8: Range of melt pool height achieved for the laser beam diameter of 43 µm as a function of the laser power and scanning speed.

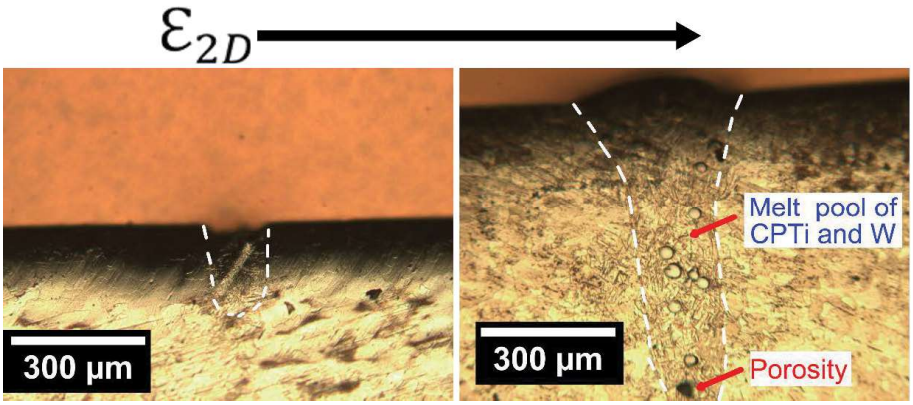

Figure 9: Optical micrographs showing the melt pool cross-sections after melting a layer of tungsten powder on a titanium substrate (focus offset=1 mm).

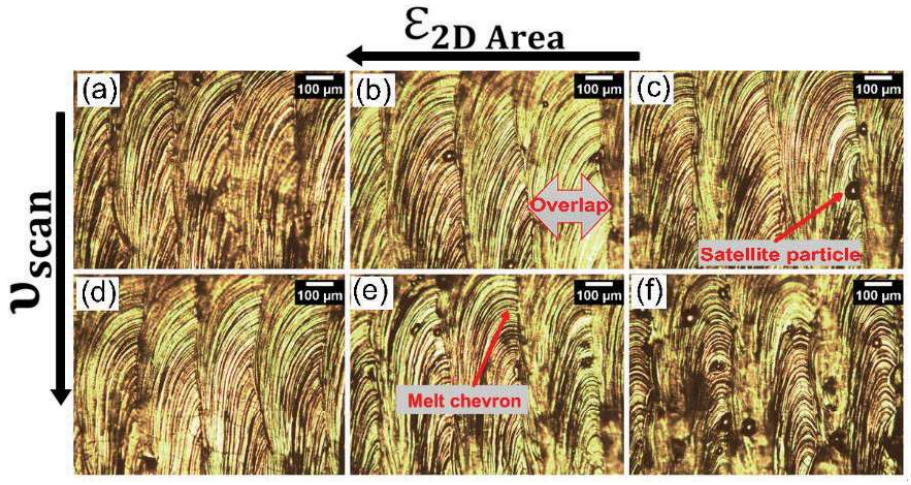

Figure 10: Optical micrographs showing melt pool overlap during LPBF. When the hatch spacing is taken into account the 2D linear laser energy density is converted into 2D area laser energy density.

When using the LPBF process for the fabrication of 3 dimensional components, the hatch spacing, and layer thickness must be taken into consideration as showed in Equation 2. The range of the melt pool width and height obtained, in combination with a melt track overlap are conditions that promote sufficient remelting of a section the previous layer, thereby expected to break down of the oxide films and remove contamination (e.g. Figure 10 (a)). The parameters may also be selected for a smooth surface topography, otherwise melt break up will take place. Figure 10 (f) indicates that insufficient overlap of the scan tracks could result in fusion defects or porosity (satellite particles). This would render it difficult to deposit subsequent layers leading to defects such as porosity and hence decreased part density.

ISBN 978-0-6398390-0-4

$$\mathcal{E}_{2D\ Area} = \frac{P_{Laser}}{\upsilon_{scan} \cdot S_{Hatch}} \qquad \text{Equation 2}$$

Where S_{hatch} = hatch spacing

4. CONCLUSION

The parameters were optimized so that the laser energy was able to create a strong bond of tungsten layer on a CPTi substrate. When the conditions were inadequate, there was breaking up of the melt pool and "balling", probably as a result of additional reduction of the surface free energy. By melting the tungsten powder on the CPTi substrate, the melting point was lowered to that of the CPTi and the thermal conductivity was expected to be lowered by not more that 25% as reported by Lukáč (Lukáč et al. [30]), which also contributed to the melt pool spreading. The increase of 2D linear energy density that was accompanied by an increase in the melt track width indicated that the melt flow dynamics analogous to the Marangoni effect were significant. At the maximum 2D linear energy density of 93 J/mm^2, the melt pool width was ~470 µm. The increase of 2D linear energy density was also accompanied by an increase in the melt pool height and penetration depth, but there was less correlation because the keyhole and conduction modes also depended on scan speed. The increased 2D linear energy densities yielded a melt pool total height was ~700 µm. The thermal effects of melting single layer and single track melt pools took into consideration the properties of CP-Ti and tungsten.

5. REFERENCES

[1] **Sidambe A.T., Tian Y., Prangnell P.B., Fox P.** 2018. Effect of processing parameters on the densification, microstructure and crystallographic texture during the laser powder bed fusion of pure tungsten, *International Journal of Refractory Metals and Hard Materials*. pp. https://doi.org/10.1016/j.ijrmhm.2018.10.004.

[2] **Sidambe A.T.** 2014. Biocompatibility of Advanced Manufactured Titanium Implants-A Review, *Materials*. 7 (12), pp 8168-88. https://doi.org/10.3390/ma7128168.

[3] **Deprez K., Vandenberghe S., Van Audenhaege K., Van Vaerenbergh J., Van Holen R.** 2013. Rapid additive manufacturing of MR compatible multipinhole collimators with selective laser melting of tungsten powder, *Med Phys*. 40 (1), pp 012501. https://doi.org/10.1118/1.4769122.

[4] **Sidambe A.T., Judson D.S., Colosimo S.J., Fox P.** 2019. Laser powder bed fusion of a pure tungsten ultra-fine single pinhole collimator for use in gamma ray detector characterisation, *International Journal of Refractory Metals and Hard Materials*. pp 104998. https://doi.org/10.1016/j.ijrmhm.2019.104998.

[5] **Braun J., Kaserer L., Stajkovic J., Leitz K.H., Tabernig B., Singer P., et al.** 2019. Molybdenum and tungsten manufactured by selective laser melting - Analysis of defect structure and solidification mechanisms, *International Journal of Refractory Metals and Hard Materials*. pp 104999. https://doi.org/https://doi.org/10.1016/j.ijrmhm.2019.104999.

[6] **Wang D.-Z., Li K.-L., Yu C.-F., Ma J., Liu W., Shen Z.-J.** 2019. Cracking Behavior in Additively Manufactured Pure Tungsten, *Acta Metallurgica Sinica (English Letters)*. 32 (1), pp 127-35. https://doi.org/10.1007/s40195-018-0752-2.

[7] **Li K., Wang D., Xing L., Wang Y., Yu C., Chen J., et al.** 2019. Crack suppression in additively manufactured tungsten by introducing secondary-phase nanoparticles into the matrix, *International Journal of Refractory Metals and Hard Materials*. 79, pp 158-63. https://doi.org/https://doi.org/10.1016/j.ijrmhm.2018.11.013.

[8] **Zhou X., Liu X.H., Zhang D.D., Shen Z.J., Liu W.** 2015. Balling phenomena in selective laser melted tungsten, *J Mater Process Tech*. 222, pp 33-42. https://doi.org/10.1016/j.jmatprotec.2015.02.032.

[9] **Wang F., Guo W., Liu J., Li S., Zhou J.** 2014. Microstructural evolution and grain refinement mechanism of pure tungsten under explosive loading condition, *International Journal of Refractory Metals and Hard Materials*. 45, pp 64-70. https://doi.org/10.1016/j.ijrmhm.2014.03.008.

[10] **Rombouts M., Kruth J.P., Froyen L., Mercelis P.** 2006. Fundamentals of selective laser melting of alloyed steel powders, *Cirp Ann-Manuf Techn*. 55 (1), pp 187-92.
[11] **Wauthle R., van der Stok J., Amin Yavari S., Van Humbeeck J., Kruth J.P., Zadpoor A.A., et al.** 2015. Additively manufactured porous tantalum implants, *Acta Biomater*. 14, pp 217-25. https://doi.org/10.1016/j.actbio.2014.12.003.
[12] **Müller A.v., Schlick G., Neu R., Anstätt C., Klimkait T., Lee J., et al.** 2019. Additive manufacturing of pure tungsten by means of selective laser beam melting with substrate preheating temperatures up to 1000 ◦C, *Nuclear Materials and Energy*. 19, pp 184-8. https://doi.org/10.1016/j.nme.2019.02.034.
[13] **Nie B., Yang L., Huang H., Bai S., Wan P., Liu J.** 2015. Femtosecond laser additive manufacturing of iron and tungsten parts, *Applied Physics A*. 119 (3), pp 1075-80.
[14] **Bai S., Liu J., Yang P., Huang H., Yang L.-M.** *Femtosecond fiber laser additive manufacturing of tungsten*. SPIE LASE: International Society for Optics and Photonics; 2016. p. 97380U-U-10.
[15] **Ivekovic A., Omidvari N., Vrancken B., Lietaert K., Thijs L., Vanmeensel K., et al.** 2017. Selective laser melting of tungsten and tungsten alloys, *International Journal of Refractory Metals and Hard Materials*. pp. https://doi.org/10.1016/j.ijrmhm.2017.12.005.
[16] **Tan C., Zhou K., Ma W., Attard B., Zhang P., Kuang T.** 2018. Selective laser melting of high-performance pure tungsten: parameter design, densification behavior and mechanical properties, *Science and Technology of Advanced Materials*. pp 1-22. https://doi.org/10.1080/14686996.2018.1455154.
[17] **Yang G., Yang P., Yang K., Liu N., Jia L., Wang J., et al.** 2019. Effect of processing parameters on the density, microstructure and strength of pure tungsten fabricated by selective electron beam melting, *International Journal of Refractory Metals and Hard Materials*. pp 105040. https://doi.org/https://doi.org/10.1016/j.ijrmhm.2019.105040.
[18] **Guo M., Gu D., Xi L., Zhang H., Zhang J., Yang J., et al.** 2019. Selective laser melting additive manufacturing of pure tungsten: Role of volumetric energy density on densification, microstructure and mechanical properties, *International Journal of Refractory Metals and Hard Materials*. pp 105025. https://doi.org/https://doi.org/10.1016/j.ijrmhm.2019.105025.
[19] **Gear J.I., Taprogge J., White O., Flux G.D.** 2019. Characterisation of the attenuation properties of 3D-printed tungsten for use in gamma camera collimation, *EJNMMI Physics*. 6 (1), pp 1. https://doi.org/10.1186/s40658-018-0238-3.
[20] **Gear J., Flux G.** *Design Optimisation of 3D Printed Parallel-Hole Tungsten Collimators for High Activity I-131 Imaging*. Annual Congress of the European Association of Nuclear Medicine. Barcelona: SPRINGER 233 SPRING ST, NEW YORK, NY 10013 USA; 2016. p. S112-S.
[21] **Sidambe A.T., Fox P.** *Interaction of pure tungsten powder with processing conditions in Selective Laser Melting*. POWDERMET2017: International Conference on Powder Metallurgy and Particulate Materials. Las Vegas, Nevada: MPIF; 2017.
[22] **Sidambe A.T., Fox P.** *Investigation of the Selective Laser Melting process with tungsten metal powder*. 19th Plansee Seminar. Reutte, Austria: Plansee; 2017.
[23] **Karapatis P.** 2002. A sub-process approach of selective laser sintering. pp.
[24] **Niu H.J., Chang I.T.H.** 1999. Instability of scan tracks of selective laser sintering of high speed steel powder, *Scripta Mater*. 41 (11), pp 1229-34. https://doi.org/10.1016/S1359-6462(99)00276-6.
[25] **Kruth J.P., Froyen L., Van Vaerenbergh J., Mercelis P., Rombouts M., Lauwers B.** 2004. Selective laser melting of iron-based powder, *J Mater Process Tech*. 149 (1-3), pp 616-22. https://doi.org/10.1016/j.jmatprotec.2003.11.051.
[26] **Guo M., Gu D., Xi L., Du L., Zhang H., Zhang J.** 2018. Formation of scanning tracks during Selective Laser Melting (SLM) of pure tungsten powder: Morphology, geometric features and forming mechanisms, *International Journal of Refractory Metals and Hard Materials*. pp. https://doi.org/10.1016/j.ijrmhm.2018.11.003.
[27] **Alda J.** 2003. Laser and Gaussian beam propagation and transformation, *Encyclopedia of optical engineering*. 2013, pp 999-1013.
[28] **Brown B.** Characterization of 304L stainless steel by means of minimum input energy on the selective laser melting platform 2014 [*Masters*]. Missouri University Of Science And Technology.
[29] **Yadroitsev I., Bertrand P., Smurov I.** 2007. Parametric analysis of the selective laser melting process, *Appl Surf Sci*. 253 (19), pp 8064-9. https://doi.org/10.1016/j.apsusc.2007.02.088.
[30] **Lukáč F., Vilémová M., Nevrlá B., Klečka J., Chráska T., Molnárová O.** 2016. Properties of Mechanically Alloyed W-Ti Materials with Dual Phase Particle Dispersion, *Metals*. 7 (1), pp 3.